Int J CARS (2017) 12:1257–1270
DOI 10.1007/s11548-017-1593-6

ORIGINAL ARTICLE

Versatile, robust, and efficient tractography with constrained higher-order tensor fODFs

Michael Ankele[1] · **Lek-Heng Lim**[2] · **Samuel Groeschel**[3] · **Thomas Schultz**[1]

Received: 2 February 2017 / Accepted: 19 April 2017 / Published online: 29 April 2017

Abstract
Purpose Develop a multi-fiber tractography method that produces fast and robust results based on input data from a wide range of diffusion MRI protocols, including high angular resolution diffusion imaging, multi-shell imaging, and clinical diffusion spectrum imaging (DSI)
Methods In a unified deconvolution framework for different types of diffusion MRI protocols, we represent fiber orientation distribution functions as higher-order tensors, which permits use of a novel positive definiteness constraint (H-psd) that makes estimation from noisy input more robust. The resulting directions are used for deterministic fiber tracking with branching.
Results We quantify accuracy on simulated data, as well as condition numbers and computation times on clinical data. We qualitatively investigate the benefits when processing suboptimal data, and show direct comparisons to several state-of-the-art techniques.
Conclusion The proposed method works faster than state-of-the-art approaches, achieves higher angular resolution on simulated data with known ground truth, and plausible results on clinical data. In addition to working with the same data as previous methods for multi-tissue deconvolution, it also supports DSI data.

Keywords Diffusion imaging · Fiber tracking · Constrained spherical deconvolution · Higher-order tensors · SHORE

Introduction

Tractography algorithms reconstruct the trajectories of major fiber bundles based on data from diffusion MRI (dMRI), and are now firmly established in neurosurgical planning [5] and studies of brain white matter [32]. It has long been known that tractography based on diffusion tensor imaging [3,16] is unable to deal with the large number of voxels in which multiple fiber populations cross or fan out. Constrained spherical deconvolution [26] is a widely used alternative that successfully reconstructs fiber crossings from high angular resolution diffusion imaging (HARDI) data.

For each voxel, spherical deconvolution computes a fiber orientation distribution function (fODF). While local fODF maxima are often taken as indicators of main fiber directions [26], previous work from ourselves and other groups [11,22,24,33] suggests that mathematically representing fODFs as higher-order tensors and performing a low-rank approximation reproduces fiber directions with increased accuracy, especially when fibers cross at small angles.

Our present work significantly extends this higher-order tensor based approach by applying a constraint that was first introduced in our recent conference publication [2]. We name this constraint H-psd, since it requires positive semidefiniteness (psd) of a matrix H that is related to the Hankel form of the higher-order tensor. It can be imposed on fODFs to make their estimation more robust, especially when only relatively

This work was supported by the DFG under Grant SCHU 3040/1-1. LHL is supported by AFOSR FA9550-13-1-0133, DARPA D15AP00109, NSF IIS 1546413, DMS 1209136, and DMS 1057064.

✉ Thomas Schultz
schultz@cs.uni-bonn.de

[1] Institute of Computer Science II, University of Bonn, Friedrich-Ebert-Allee 144, 53113 Bonn, Germany

[2] Department of Statistics, University of Chicago, 5747 S Ellis Ave, Chicago, IL 60637, USA

[3] Department of Pediatric Neurology and Developmental Medicine and Experimental Pediatric Neuroimaging, University Children's Hospital Tübingen, Tübingen, Germany

little or noisy dMRI data are available. Its benefit is analogous to the addition of a nonnegativity constraint [26] to the original spherical deconvolution approach [28], which has greatly increased its practical utility. However, our H-psd constraint is stronger than nonnegativity, and its exact mathematical motivation and implementation are substantially different. This is the first part of our technical contribution.

Spherical deconvolution has recently been extended to work with multi-shell data, i.e., dMRI data which have been acquired at multiple levels of diffusion weighting [10]. In regions of partial voluming between white and gray matter or corticospinal fluid, this makes it possible to isolate the part of the dMRI signal corresponding to white matter, which makes tractography in those regions more robust. As a second contribution, we present a unified framework that allows us to apply this idea also to diffusion spectrum imaging (DSI). The traditional algorithms used to perform tractography based on DSI data [4,30] are different from those commonly used on HARDI and multi-shell data, and our experimental results provide a direct comparison.

Methods

Our proposed method supports single tissue, as well as multi-tissue deconvolution. "A unified deconvolution framework" Section describes our unified framework that permits multi-tissue deconvolution even in cases where measurements include multiple levels of diffusion weighting, but are not organized on shells. Our H-psd constraint, which makes deconvolution numerically more robust, is explained in "Constrained higher-order tensor fODFs" Section, with mathematical details given in an appendix. Finally, "Deterministic tractography with branching" Section describes the fiber tracking algorithm used in our experiments.

A unified deconvolution framework

Single tissue deconvolution is based on the assumptions that, up to rotations that account for differences in orientation, all fibers within a voxel give rise to the same dMRI signal, and that signals from differently oriented fibers add up linearly. Under these conditions, in voxels that contain only white matter, the measured dMRI signal can be expressed as a convolution integral on the sphere. In particular, a fiber orientation distribution function (fODF) that captures the fraction of fibers in each direction is convolved with a kernel that reflects the common dMRI response from a single, coherently oriented fiber compartment [28]. fODFs are antipodally symmetric and do not indicate the direction of signal transmission along the bundle; in accordance with the literature, we use the terms "direction" and "orientation" interchangeably.

Multi-tissue deconvolution involves multiple tissue response functions [7,10]. It has mostly been used to separate out signal contributions from gray matter (GM) and corticospinal fluid (CSF), which have been modeled as isotropic, and therefore only add respective volume fraction parameters, rather than additional fODFs. These tissue types are distinguished based on differences in how their dMRI signal is attenuated at different levels of diffusion weighting, which are commonly quantified as b values. Previous approaches [7,10] employ separate response functions for each tissue and each distinct b value. This is well-suited for multi-shell data, in which the full space of orientations is sampled for each of a small number of different b values.

When using Diffusion Spectrum Imaging [31], or some recently proposed dMRI protocols that distribute samples freely in q-space [13,18], many different b values are available, but with few or even only a single orientation each. In this case, modeling independent spherical functions for each b value results in an unreasonably large number of model parameters. An immediate consequence is that the previously proposed method for response function estimation [10] cannot be used on such data.

Therefore, our unified framework for multi-tissue deconvolution instead builds on a continuous model of functions $F(\mathbf{q} = q\mathbf{u})$ in q-space, using the SHORE basis functions [15]

$$\begin{aligned}\phi_{lnm}(\mathbf{q}) &= \left[\frac{2(n-l)!}{\zeta^{3/2}\Gamma(n+3/2)}\right]^{1/2}\left(\frac{q^2}{\zeta}\right)^{l/2} \\ &\quad\times \exp\left(\frac{-q^2}{2\zeta}\right)L_{n-l}^{l+1/2}\left(\frac{q^2}{\zeta}\right)Y_l^m(\mathbf{u}) \qquad (1)\end{aligned}$$

with the associated Laguerre polynomials L_n^α, the real spherical harmonics Y_l^m, and a radial scaling factor $\zeta = 700$. We use maximum radial and angular orders four, which leads to a fixed number of 6 parameters to describe a cylindrically symmetric white matter response function, while per-shell modeling as in [10], even when reducing the angular order to four, would still require $1 + 3 \times B$ parameters, where B is the number of unique nonzero b values, e.g., $B = 16$ in the DSI data used in our experiments.

Let $K(\mathbf{q}) = \sum_{ln} K_{ln}\,\phi_{ln0}(\mathbf{q})$ be the white matter single fiber response, with $m = 0$ due to cylindrical symmetry. The signal from an fODF f is then modeled by a convolution on the sphere, $S(\mathbf{q}) \approx K \star_{\mathbb{S}^2} f$ [6]. For a given K and signal vector $S_i = S(\mathbf{q}_i)$, finding the spherical harmonics coefficients f via deconvolution becomes a linear least squares problem:

$$\operatorname{argmin}_f \|Mf - S\|^2 \qquad (2)$$

with convolution matrix

$$M_{(i)(lm)} = \sum_n \frac{1}{\alpha_l} K_{ln}\,\phi_{lnm}(\mathbf{q}_i). \qquad (3)$$

Tournier et al. [26] constrain the optimization in Eq. (2) by requiring f to be nonnegative and define the α_l in Eq. (3) from the truncated spherical harmonics transform of the unit delta function. Our method improves numerical stability by making these two choices differently, as will be explained in "Constrained higher-order tensor fODFs" Section.

Multi-tissue support is added by concatenating individual tissue matrices

$$M = [M_{\mathrm{CSF}}, M_{\mathrm{GM}}, M_{\mathrm{WM}}], \quad f = \begin{bmatrix} f_{\mathrm{CSF}} \\ f_{\mathrm{GM}} \\ f_{\mathrm{WM}} \end{bmatrix}. \tag{4}$$

Since CSF and GM are isotropic, M_{CSF} and M_{GM} are single-column matrices. Given single-shell data, multiple tissues cannot be estimated. In this case, we simply replace the SHORE with the spherical harmonics basis, which leads to omission of the radial parameter n from Eq. (3).

Tissue response functions are estimated in close analogy to a previous method for multi-tissue deconvolution [10]: Initial masks for WM, GM, and CSF are created from an intensity-based tissue segmentation of a coregistered T_1 image [34], thresholded at 95% for each tissue type. These masks are refined based on Fractional Anisotropy (FA) from a diffusion tensor fit, by restricting them to FA > 0.7 for core white matter, and FA < 0.2 for GM and CSF. SHORE coefficients of the three response functions are obtained by fitting and averaging within the respective masks. Due to the stringent FA threshold, the core white matter mask is thought to contain voxels with a single dominant fiber in each. They were aligned by rotating the principal eigenvector of the diffusion tensor to the z axis, which was achieved by rotating the B matrix before the SHORE fit.

Constrained higher-order tensor fODFs

In a previous work [24], we proposed to describe fODFs f by fully symmetric fourth-order tensors:

$$f(\mathbf{v}) = T(\mathbf{v}) = \sum_{i,j,k,l=1}^{3} T_{ijkl}\, v_i v_j v_k v_l, \quad \mathbf{v} \in \mathbb{S}^2 \tag{5}$$

Such fODF tensors T are obtained by deconvolution in the Spherical Harmonics basis, as in Eq. (2), and subsequently changing to the monomial basis, which can be done using a nonsingular linear transformation [17]. In the higher-order tensor framework, it is natural to represent a single fiber contribution with volume fraction λ in unit direction $\mathbf{u}$ as a rank-one tensor $\lambda \mathbf{u} \otimes \mathbf{u} \otimes \mathbf{u} \otimes \mathbf{u}$, which can be achieved by setting the α_l in Eq. (3) to the spherical harmonics coefficients of a unit rank-1 tensor. In the resulting representation, k principal fiber directions for deterministic tractography should be extracted from an fODF by performing a symmetric rank-k approximation, rather than using the k dominant peaks of the fODF function [11,24].

A key technical contribution of our current work is to formulate a constraint which we call H-psd. It is the suitable higher-order tensor counterpart of the nonnegativity constraint on f that is commonly imposed in Eq. (2) [26]. It can be enforced in an exact, simple, and efficient manner using standard optimization packages, and it is theoretically well-founded in the sense that it can be shown to be equivalent to the condition that a valid fODF should represent a mixture of nonnegative fiber compartments. It is more rigorous than nonnegativity in the sense that any H-psd fODF is nonnegative, but the reverse may not be true: Intuitively, some nonnegative fODFs are so sharp that they cannot possibly arise from a nonnegative mixture of fiber compartments, which have a minimum width in the higher-order tensor framework.

Since the exact mathematical derivation of the H-psd constraint will only be relevant to part of the intended audience of our work, we present it in an appendix. The main result, which also explains the name H-psd, is the fact that the matrix H in Eq. (18), which is composed of the coefficients of T, has to be positive semidefinite (psd).

In practice, this constraint can be imposed on Eq. (2) using the quadratic cone program (QCP)

$$\operatorname{argmin}_f \frac{1}{2}\langle f, Pf\rangle + \langle q, f\rangle \quad \text{subject to} \quad (Gf)\ \text{psd} \tag{6}$$

with f, M and S as in Eq. (2), $P = M^T M$, $q = -M^T S$, and a matrix G that first maps f from spherical harmonics to the monomial basis, and then to its H matrix from Eq. (18), $Gf = H_f$. In multi-tissue deconvolution, additional nonnegativity constraints are enforced for f_{GM} and f_{CSF}.

The QCP is solved using the routine CONEQP in the publicly available software package CVXOPT, which requires the above-mentioned vectors and matrices as its only input. Details on its implementation are given in [29], and are beyond the scope of our paper.

Deterministic tractography with branching

Similar to previous work [8,24,27,30], deterministic multi-fiber tractography has been implemented with Euler integration. In each of the local fiber directions at a given seed point, a streamline is extended bi-directionally with an integration stepsize that was set to 0.5 mm in our experiments. In each integration step, a local fODF is interpolated trilinearly, and a set of fiber directions is extracted from it. In case of multiple options, the fiber direction that leads to lowest tract curvature is selected.

Streamline integration stops when no fiber is found within a given turning angle (exact values specified below), after a

maximum number of integration steps (400), or when the white matter volume fraction was below 0.5. This volume fraction is estimated by the multi-tissue deconvolution itself or, in case of single-shell data, using a coregistered T_1 tissue segmentation.

In order to capture the effect of fiber dispersion, we implement branching. In particular, when multiple directions are permissible, the tract branches out, i.e., a new streamline is seeded in the direction leading to the second lowest curvature. In order to avoid excessive branching, streamlines that result from branching are not allowed to branch again, and the original ones can only branch again after some number of integration steps (4 mm).

In our framework, main fiber directions are extracted using low-rank approximation, which requires deciding on a suitable number k of local fiber compartments. As discussed more formally in the appendix, k amounts to the numerical rank of the fODF tensor, which coincides with the rank of the same matrix H that underlies the H-psd constraint. Therefore, we estimate k as the number of eigenvalues of H above some threshold θ. Since we are not aware of any regions where more than three fiber tracts cross, we impose a maximum of $k \leq 3$. We found that the exact values of θ that lead to plausible results depended on the acquisition scheme and regularization. We set it by visually inspecting the spatial maps of the number of fiber compartments resulting from different choices, and report values for the individual experiments below. Rank-one terms with scaling factor $\lambda_i < 0.15$ were discarded.

For comparison, we also created results using methods that take local fODF maxima as estimates of main fiber directions. In this case, we first roughly localize local maxima on a discretization of the sphere (321 unique directions), and subsequently refine their exact positions using gradient ascent. Peaks with magnitude below 0.1 were discarded.

Results

We report results of our method on two clinical dMRI datasets, and on data that we synthesized from one of them, as described in "Simulation Experiment" Section. Motion correction was performed in a preprocess using the tools available in FSL [1].

The first dataset, *clin-2-sh,* is a two-shell dataset from a healthy volunteer, measured on a 3T Skyra (Siemens, Germany) with $96 \times 96 \times 50$ voxels of 2 mm isotropic size, TE/TR = 89/9100 ms. Three images were taken at $b = 0$, 30 DWIs at $b = 700$, and 64 at $b = 2000$ (all b values in s/mm^2). Some experiments only use the data from the inner or outer shell (*clin-700* and *clin-2000,* respectively). We note that traditional single-shell deconvolution does not make use of the $b = 0$ images.

The second dataset, *clin-dsi,* was kindly provided by Katrin Sakreida and Georg Neuloh (RWTH Aachen University Hospital). It was acquired on a 3T Prisma (Siemens, Germany) with $136 \times 136 \times 84$ voxels of 1.5 mm isotropic size, TE/TR = 69/11600 ms. One $b = 0$ image and 128 DWIs with b values up to $b = 3000$ were taken on a Cartesian grid.

Simulation experiment

In order to quantify the accuracy of our method, we generate dMRI data for which volume fractions and orientations of crossing fiber compartments are known. Crossings are simulated based on resampling the clinical data *clin-2-sh.* This process avoids potentially oversimplifying assumptions in mathematical models of water diffusion and noise.

Data were generated based on the same voxels used to estimate response functions for the three tissue types, as explained in "A unified deconvolution framework" Section. The respective white matter voxels are thought to contain a single fiber compartment, whose orientation was estimated via the diffusion tensor model.

For each simulated fiber crossing, we averaged the signals from two randomly chosen single fiber voxels, after applying a random rotation to them, and one voxel from either the gray matter or CSF mask. The respective volume fractions were selected randomly, and normalized to sum to one. In the presence of noise, we cannot expect any algorithm to reconstruct the orientation of fibers with a very small volume fraction. Therefore, we discarded samples in which the weaker fiber contributed less than 20% to the white matter, or in which both fibers combined accounted for less than 50% of the voxel.

We used different deconvolution approaches to reconstruct the fiber directions and volume fractions from the resulting data, and compared the results to the known values, which were recorded during the simulation. Figure 1 plots the average angular error in the reconstructed fiber directions (top) and the average absolute errors in their estimated volume fractions (bottom), each as a function of the ground truth crossing angle between the two fibers.

The scaling parameters λ_i of the low-rank approximation were directly taken as estimates of the corresponding fiber volume fraction, as motivated in "Constrained higher-order tensor fODFs" Section. When extracting fiber directions from ODF peaks (in "SH-4 delta nonneg" and "SH-8 delta nonneg"), volume fraction estimates were obtained by dividing the magnitude of the corresponding peak by the peak magnitude observed when applying constrained deconvolution of the same order to the single fiber response.

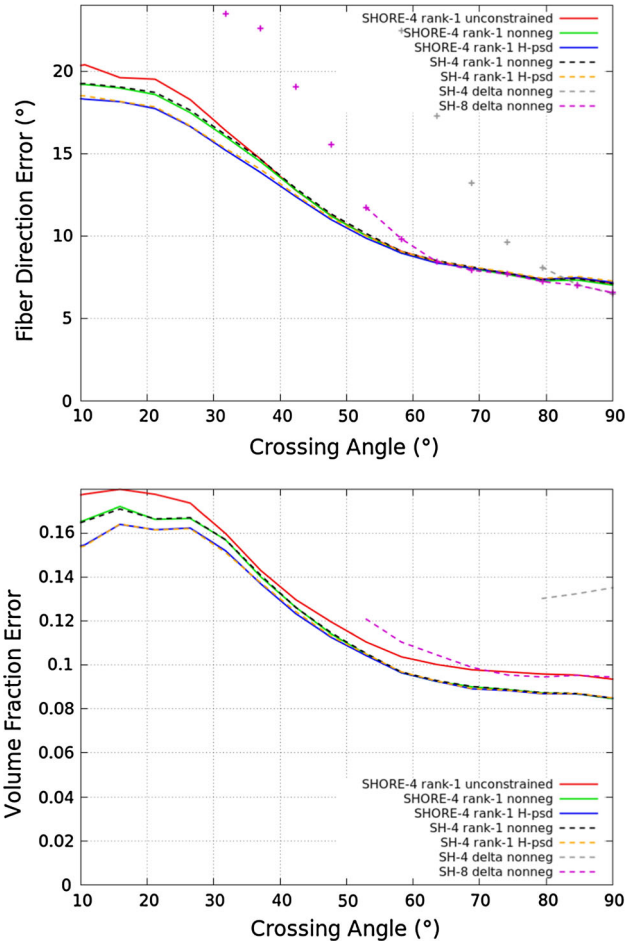

Fig. 1 Average errors of fiber directions and individual fiber volume fractions reconstructed from two-fiber crossings that have been simulated from clinical two-shell data. The proposed method is SHORE-4 rank-1 H-psd, the current state-of-the-art is SH-8 delta nonneg. Results from several hybrid methods are shown to assess the impact of individual factors

The main comparison is between our proposed method ("SHORE-4 rank-1 H-psd") and the previous state-of-the-art [10] ("SH-8 delta nonneg"). We note that, for angles smaller than approximately 55°, the latter method no longer reliably resolved the crossing, with two significant fODF peaks being detected in less than 50% of the cases. We continue to show fiber direction errors based on the remaining few cases as isolated markers.

In order to investigate the effects of individual factors that make up the difference between our method and the previous state-of-the-art, we also performed experiments with several hybrid methods, including one that combines lower order with peak finding ("SH-4 delta nonneg"), ones that use traditional per-shell signal modeling instead of the SHORE basis ("SH" variants of "SHORE"), or replace our H-psd with a traditional nonnegativity constraint in 300 discrete directions [26].

Single-shell deconvolution

Similar to Tournier et al. [26], who demonstrate that their nonnegativity constraint allows them to produce plausible results even with relatively low b value and few gradient directions, we test our H-psd constraint by applying it to *clin-700* (30 DWIs at $b = 700$). Figure 2 visualizes the resulting fODFs and a deterministic streamline tractography in the brainstem region.

Unlike the standard diffusion tensor model, which is shown for comparison, combining spherical deconvolution with low-rank approximation allows us to reconstruct pontine crossing tracts even with this limited b value and number of gradient directions (maximum turning angle 40°; $\theta = 0.35$ for unconstrained, $\theta = 0.1$ for H-psd). Negative values of the fODFs are shown in white in Fig. 2b. They are removed, and fODFs in adjacent voxels become more similar, when enforcing the H-psd constraint.

For comparison, Subfigure (e) shows results based on *clin-2000* (64 DWIs at $b = 2000$; $\theta = 0.1$), which is commonly considered a more suitable input for spherical deconvolution [26]. Subfigures (d) and (f) provide a direct comparison with classical constrained spherical deconvolution (CSD).

Table 1 compares the times for whole-brain deconvolution, measured on a workstation with a six-core CPU at 3.4 GHz, and using the same optimization package (CVXOPT) for all methods. Our method takes only about half as long as CSD, mostly due to our use of a lower model order. In Fig. 2, this is reflected in the increased smoothness of our fODFs. Despite this, applying low-rank approximation allows us to obtain very similar tractography results.

In addition to the reduced computational effort for whole-brain deconvolution, tractography is also less costly when using order-4 low-rank approximation, compared to order-8 peak finding: In our implementation, one integration step with the former took 16 ms on average, while one step with the latter took around 125 ms.

While the H-psd constraint improves the results of fourth-order tensor-based deconvolution, Fig. 2b shows that we achieve useful results even without it, even on the *clin-700* data. This is in contrast to standard order-8 deconvolution, whose results without enforcing nonnegativity were dominated by noise so severely, even in the *clin-2000* data, that it did not make sense to present them. This is explained by inspecting the condition number of the matrix P that defines the respective quadratic optimization, listed in Table 2. Estimating order-8 fODFs from *clin-700* is an underdetermined problem, represented symbolically in Table 2 by an infinite condition number. As we saw in Fig. 1, order-4 variants of standard deconvolution do not provide a useful angular resolution. We still include them in the final row of Table 2 to illustrate that the improved conditioning of our method is only partially explained by the reduced model order. Using

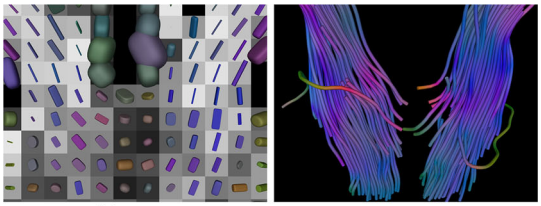

(a) Diffusion Tensors, 30 DWIs, $b = 700$

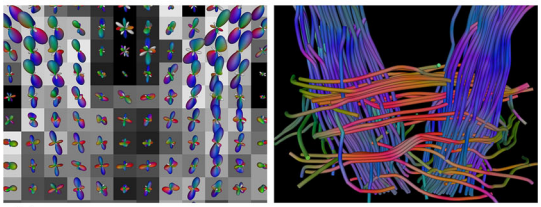

(b) Tensor-based fODFs, unconstrained, 30 DWIs, $b = 700$

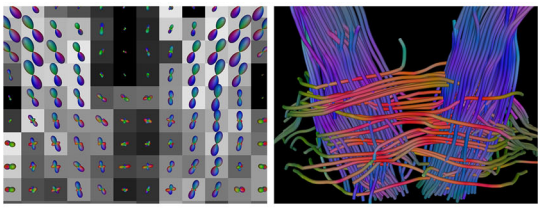

(c) Tensor-based fODFs, H-psd, 30 DWIs, $b = 700$

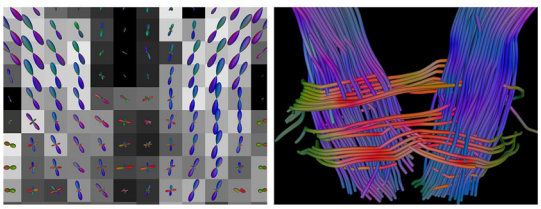

(d) Classical CSD fODFs, 30 DWIs, $b = 700$

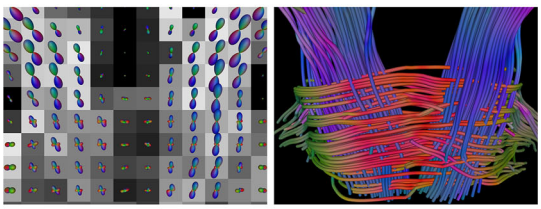

(e) Tensor-based fODFs, H-psd, 64 DWIs, $b = 2000$

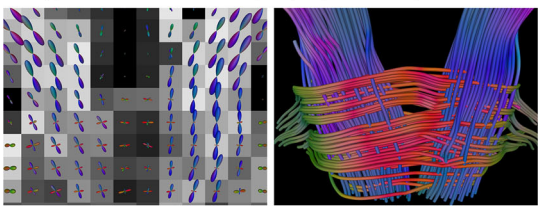

(f) Classical CSD fODFs, 64 DWIs, $b = 2000$

Fig. 2 Unlike diffusion tensors (**a**), fODFs allow us to resolve the pontine crossing tracts. In **c**, our H-psd constraint reduces the impact of noise and removes negative fODF lobes, shown in white in the left part of (**b**). Even though it is possible to reconstruct fiber crossings even from few gradient directions at low b values, cleaner results are obtained when HARDI data are available, as shown in (**e**) and (**f**). We achieve similar tractography as classical CSD, at a reduced computational cost

a rank-1 representation of single fibers, as it was introduced in "Constrained higher-order tensor fODFs" Section, also improves conditioning considerably.

In theory, our H-psd constraint forces fODFs to be nonnegative everywhere, while standard CSD [26] only enforces nonnegativity in 300 discrete directions. We quantified to which extent our numerical implementations of both constraints satisfy nonnegativity in practice. This was done by evaluating ODFs along a dense set of 1281 unique directions, and taking the minimum of all results. Computed over the whole-brain estimates in *clin-700,* a minimum of -1.38×10^{-7} indicated a negligible numerical inaccuracy in enforcing the H-psd constraint. Even though we used the capabilities of CVXOPT to enforce nonnegativity in 300 directions as hard constraints, as opposed to implementing soft constraints as proposed in [26], the minimum ODF value observed for classical CSD was much more substantial, -0.164.

Multi-shell deconvolution

Using all data from *clin-2-sh,* we compared results from state-of-the-art multi-shell multi-tissue deconvolution [10], which involves order-8 fODFs based on the truncated delta peak and a nonnegativity constraint, to our proposed method, which uses a fourth-order tensor representation of fODFs with our H-psd constraint.

We found the tissue volume fraction maps from both methods, shown in Fig. 3, to be quite similar. Averaged over a brain mask, the mean absolute difference was 0.005 in CSF, 0.026 in gray matter, and 0.025 in white matter. As in Fig. 2, our fODFs are less sharp compared to the ones from the existing approach [10]. The bottom row of Fig. 3 shows that low-rank approximation allows us to resolve two and three fiber crossings despite the smoothness of our fODFs. Averaged over the white matter, the angular deviation, weighted by volume fractions, was 8.24° when comparing fiber directions from order-8 fODF peaks to the results of fourth-order low-rank approximation.

Similar to previous work on crossing fiber tractography [14,24], we compared the ability of different fiber tracking algorithms to reliably reconstruct transcallosal fibers from seeds in the corpus callosum near the mid-sagittal plane. The left column of Fig. 4 shows results from our own implementation of deterministic tractography with branching (maximum turning angle 45°, $\theta = 0.02$). It finds many lateral projections when using fiber estimates from fourth-order low-rank approximation (top), but only very few based on the peaks in traditional order-8 fODFs (bottom).

For comparison, we reprocessed the same data with the software package MRTRIX3 [27], which includes a reference implementation of the original multi-shell multi-tissue deconvolution approach [10]. In order to make the results of tracking methods with and without branching more comparable, we varied the number of tracts per seed voxel to achieve a similar final number of displayed fibers (around 4400) in

Table 1 Computation times for deconvolution of whole-brain data using different approaches, all implemented in the same optimization framework

	clin-700	clin-2000	clin-2-sh	clin-dsi
Proposed method	1m49s	1m26s	2m10s	4m45s
Order-8 CSD [26]	3m08s	3m19s	N/A	N/A
MSMT deconvolution [10]	N/A	N/A	4m10s	N/A

This does not include tractography, whose computational cost is also reduced by using low-rank approximation

Table 2 The condition numbers of the matrices defining the quadratic optimization problem in our method are much lower than in competing ones

	clin-700	clin-2000	clin-2-sh	clin-dsi
Proposed method	189	7.86	458	536
Order-8 CSD [26]	∞	3.22×10^6	N/A	N/A
MSMT deconvolution [10]	N/A	N/A	1.02×10^7	N/A
Order-4 CSD/MSMT	1.18×10^4	478	1.47×10^3	N/A

all cases. We used the recommended default step sizes with MRTRIX, which depend on the algorithm.

Since the deterministic tracking in MRTRIX does not implement branching, it finds even fewer lateral projections (bottom right). However, it includes a probabilistic tractography approach [25] that is based on sampling the fODFs rather than finding their maxima, and extracts lateral fibers similar to the ones found by our deterministic technique (top row), albeit with the increased wiggling that is characteristic of probabilistic tracking.

Clinical DSI

After applying our variant of multi-tissue deconvolution to clinical DSI data *(clin-dsi),* we evaluated the extent to which the resulting fODFs allow us to reconstruct the corticospinal tract from seeds in the internal capsule. A similar task was recently used by others to evaluate crossing fiber tractography [5]. The results are shown in the top row of Fig. 5, and are compared to results from standard DSI reconstruction [30], as implemented in the open-source software package DIPY [9].

In contrast to the fiber ODFs (fODFs) from our method, traditional DSI reconstruction results in diffusion ODFs (dODFs) that reflect the fraction of diffusion that happens in each direction, as opposed to the fraction of fiber bundles. As can be seen in the center row of Fig. 5, dODFs are generally less sharp then fODFs. Canalez-Rodríguez et al. [4] have used deconvolution to compute sharper ODFs from DSI data. The results from their method, again using the publicly available implementation from DIPY, is shown in the right-hand column of Fig. 5. We note that in contrast to our method and related ones [10], their deconvolution approach avoids assumptions on the response of single fiber compartments, and therefore does not produce fODFs.

All tractography results in Fig. 5 have been obtained with the algorithm from "Deterministic tractography with branching" Section (maximum turning angle 50°). It is using fiber estimates from low-rank approximation ($\theta = 0.02$) in case of our fODFs, and local maxima in case of dODFs, as is customary in standard DSI tractography [30]. Corresponding directions are visualized in the final row of Fig. 5. In all cases, streamlines that cross the mid-sagittal plane have been removed in a postprocess.

Discussion

Our proposed method differs from the previous state-of-the-art in several aspects, which we will discuss separately.

Unified deconvolution framework

The main benefit of our unified deconvolution framework is the fact that it allows us to perform multi-tissue deconvolution also on dMRI data that include multiple b values, but is not organized on shells. The comparison in Fig. 5 confirms that this extension of multi-tissue deconvolution produces plausible results on clinical DSI data, and compares favorably to standard DSI processing in its ability to reconstruct also the lateral projections of the cortico-spinal tract from seeds in the internal capsule.

In Fig. 5, a previously proposed method for DSI deconvolution led to an implausibly low number of secondary fiber directions in a known fiber crossing region, and decreased our ability to reconstruct branching fibers. This might indicate that the characteristics of the *clin-dsi* data, which include fewer measurements and lower maximum b value than the data used by Canalez-Rodríguez et al. [4], might be less suitable for that approach. Due to the long computational times of its DIPY implementation, we only tried it with default parameters.

The simulation results in Fig. 1 indicate that, in case the input data are organized on shells, it makes very little dif-

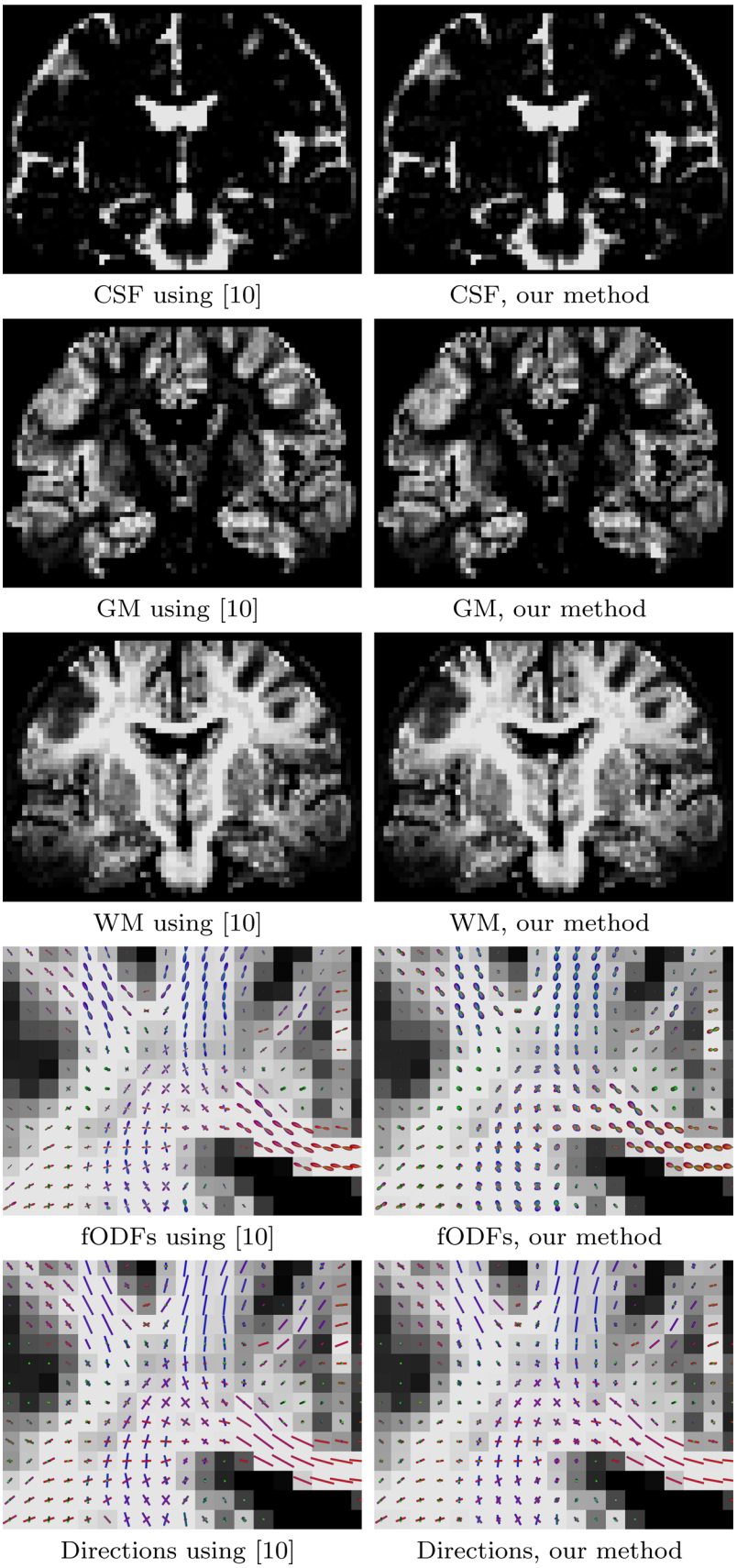

Fig. 3 On two-shell clinical data, very similar tissue volume fraction maps are obtained using a state-of-the-art approach (*left column*) and ours (*right column*). Our fODFs (fourth row) are smoother, which accounts for the improved speed and conditioning of our method. The final row (*right column*) shows that low-rank approximation allows us to reliably resolve crossing fibers directions despite the smoothness of our fODFs

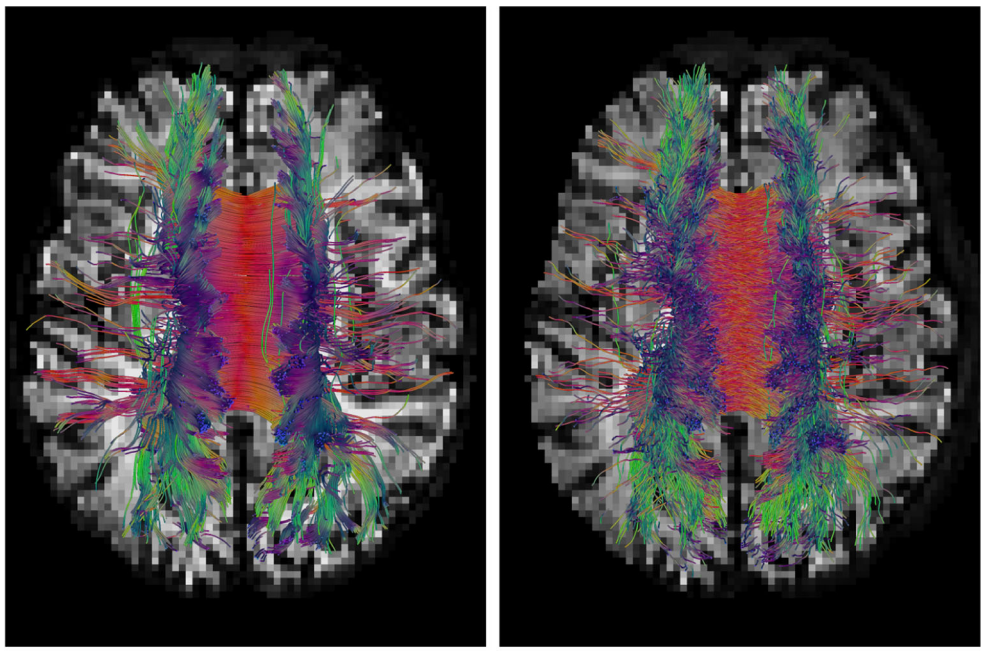

Deterministic tracking with low-rank approximation (order 4)

Probabilistic tracking (order 8)

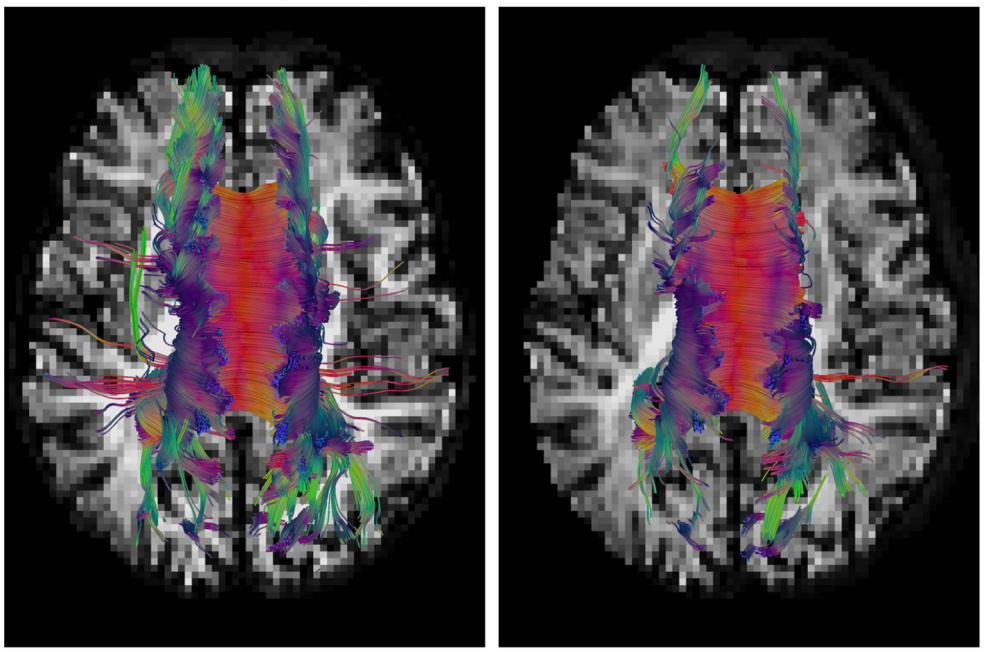

Deterministic tracking with peak finding and branching (order 8)

Deterministic tracking with peak finding, reference implementation (order 8)

Fig. 4 Our deterministic tractography based on low-rank approximation successfully reconstructs transcallosal fibers from seeds near the mid-sagittal plane. Using previously available tools, we only managed to reconstruct them with probabilistic tracking. As shown on the bottom row, deterministic tracking based on peak finding reconstructs much fewer of them, both with our own implementation (*left*) and a publicly available one (*right*)

ference whether we model the response functions per-shell, as in [7,10], or with our unified framework. Despite the fact that the angular part of the SHORE basis in Eq. (1) consists of spherical harmonics, i.e., the same basis that is otherwise used for per-shell modeling, this result is not trivial: Our approach reduces the number of parameters needed to represent the response function by assuming that radial and angular parts factorize, which is not enforced by the more flexible per-shell modeling. The fact that both methods produced almost identical results suggests that this assumption

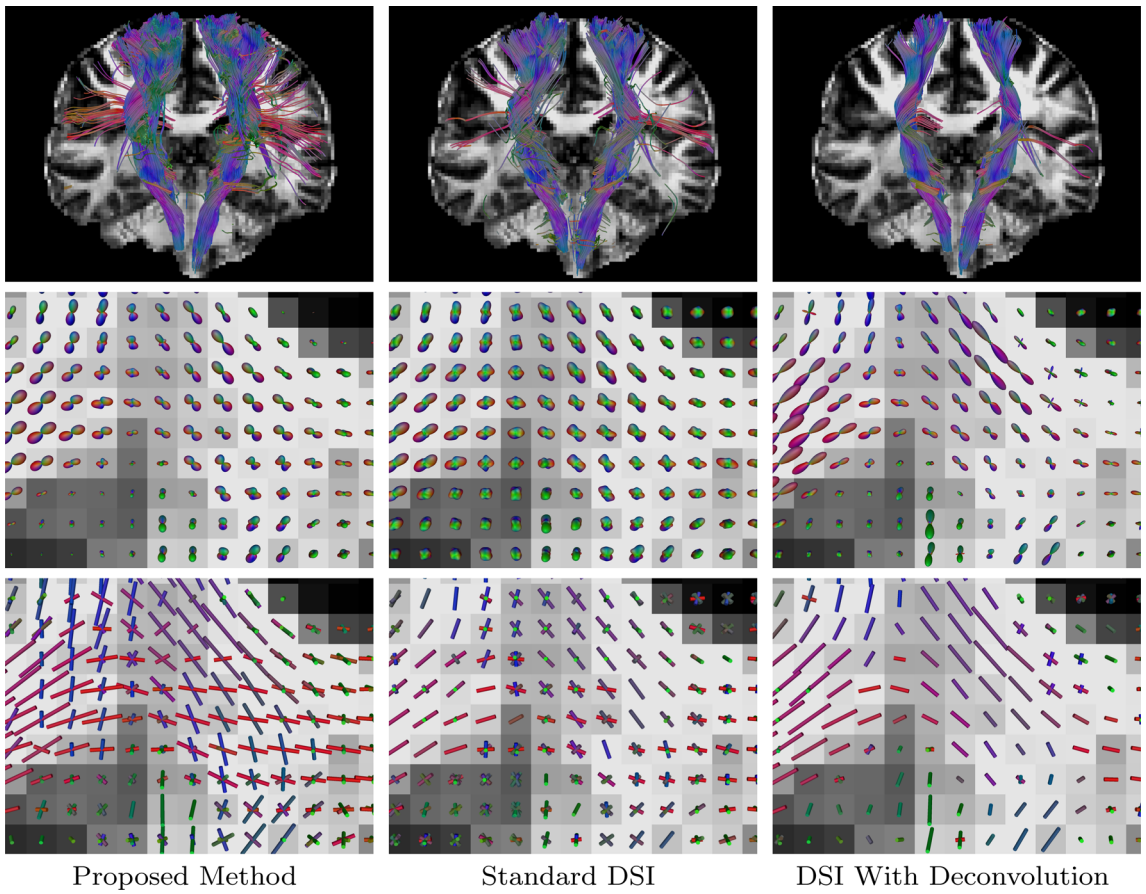

Fig. 5 Our method can also be applied to clinical DSI data, and reconstructs more lateral projections than standard DSI tools when tracking the corticospinal tract from seeds in the internal capsule. The reason for this becomes apparent when comparing fODFs from our method to dODFs from DSI (*middle row*), and the directions resulting from low-rank approximation or peak finding, respectively (*last row*)

is not violated to an extent that it would impair the deconvolution.

H-psd constraint

A theoretical benefit of our H-psd constraint is the fact that it is easy to enforce exactly, while nonnegativity is either approximated by enforcing it on a discrete set of points on the sphere [26], or requires a costly Riemannian gradient descent [6]. It was confirmed visually and quantitatively in Sect. 3.2 that enforcing H-psd removes nonnegative fODF lobes, and makes the fODFs and resulting tractography more regular.

Even though this constraint is beneficial, Fig. 1 suggests that it results in an increased accuracy mostly at small crossing angles. Clearly, constraining deconvolution based on fourth-order tensors is not as crucial as enforcing nonnegativity in order-8 CSD. This can be understood from the greatly reduced condition numbers, which were presented in Table 2, and which are made possible not only by the reduction in model order, but also by representing single fibers as rank-one tensors rather than truncated delta peaks.

A direction that we would like to follow in our future work is the use of our H-psd constraint to prevent overfitting of misspecified deconvolution models, e.g., ones that assume a response function that has been derived from healthy tissue, and may not match the true response in regions that suffer from demyelination [23].

Model order and low-rank approximation

An obvious factor that contributes to the improved conditioning and speed of our method is the fact that we use a lower order representation of fODFs, i.e., order-4 with just 15 degrees of freedom, compared to the more common order-8 models with 45 degrees of freedom. It is well-known that lower orders lead to better numerical behavior, while higher orders are commonly selected to increase angular resolution, defined as the minimum angle at which two crossing fiber populations can still be reliably distinguished [26].

At this point, the use of low-rank approximations to extract fiber directions from fODFs is the key ingredient of our method. It can be seen from Fig. 1 that low-rank approxima-

tion of a fourth-order fODF leads to an even higher angular resolution than extracting peaks of an order-8 fODF, and that reducing the order in a peak finding approach would lead to unacceptably poor resolution. Even though we demonstrated this benefit of low-rank approximations before [24], we previously compared to filtered spherical deconvolution [28], while our current work shows that the advantage is maintained compared to state-of-the-art constrained deconvolution [26].

It was shown in Fig. 1 that fiber volume fraction estimates from low-rank approximation are more accurate than ones based on ODF peak magnitudes. The reason for this is the same as for the increased angular resolution: Unlike simple maximum finding, low-rank approximation amounts to an optimization that correctly accounts for the interference of ODF peaks from mixing fibers [24]. We note that, in any case, volume fraction estimates derived from deconvolution will be affected by potential mismatches between the deconvolution kernel and the actual tissue characteristics [19].

As shown in [24], it is possible to generalize the tensor-based approach to orders higher than four. According to Eq. (26) in the appendix, the corresponding H-psd constraints are stricter than requiring nonnegativity of the fODF, but no longer ensure that the fODFs will be a mixture of nonnegative fiber contributions. Preliminary experiments, whose results are not shown, indicate that the additional benefits of taking the tensor-based approach to higher orders appear to be marginal, while the increase in computational effort is significant. Future work might investigate this in more detail.

Multi-fiber tractography

Several approaches to multi-fiber tractography are based on the idea that estimating multiple fiber directions in each voxel independently is not reliable enough, and should be regularized by using information from spatial neighborhoods. Examples include unscented Kalman filters [5,14] or global optimization frameworks [20]. Other authors have argued that a larger number of plausible tracts can be reconstructed by moving from deterministic to probabilistic tractography [27].

Our results have been achieved by improving the per-voxel estimates used within a deterministic streamline-based tractography algorithm whose benefits include its simplicity and speed. In Fig. 4, the improved angular resolution of our technique allowed us to reconstruct deterministic tracts that otherwise would have required probabilistic tracking. A comprehensive comparison of deterministic branching and probabilistic tracking as strategies for capturing the full extent of dispersing bundles will require a separate study. Similarly, it is an obvious question for future work to which extent results can be further improved by integrating our refined per-voxel estimates into more complex tractography algorithms.

Of course, many of the well-known limitations that are shared by all dMRI-based fiber tractography approaches also apply to our proposed method, and results should be interpreted with due care [12]. This includes the possibility of false positives and false negatives, i.e., missing or spurious fibers. While theoretically justified constraints such as our H-psd can contribute to reducing them, and to generating tractography that is more helpful for neurosurgery and scientific investigation, it is unclear whether this fundamental issue can be fully resolved, given the gap in spatial scales between individual axons and MR image resolution.

Conclusion

We have introduced a multi-fiber tractography method that is based on a unified deconvolution framework for HARDI, multi-shell, and diffusion spectrum imaging data, and makes use of fourth-order tensor-based deconvolution with a novel and theoretically justified H-psd constraint. Results indicate that our method is faster and numerically more robust than previous alternatives, achieves higher angular resolution on simulated data, and compares favorably to existing techniques in qualitative comparisons on clinical data. Despite the promising results, more extensive validation should be performed before our method is used in clinical practice.

Acknowledgements This work was supported by the DFG under Grant SCHU 3040/1-1. LHL is supported by AFOSR FA9550-13-1-0133, DARPA D15AP00109, NSF IIS 1546413, DMS 1209136, and DMS 1057064.

Compliance with ethical standards

Conflict of interest The authors declare that they have no conflict of interest.

Ethical approval All procedures performed in studies involving human participants were in accordance with the ethical standards of the institutional and/or national research committee and with the 1964 Helsinki Declaration and its later amendments or comparable ethical standards. The study was approved by the local ethics committee. All volunteers gave their written informed consent for participation in the study.

Appendix: Mathematical derivation of H-psd constraint

This appendix presents the formal definition of our H-psd constraint (Definition 4), based on a matrix representation H of higher-order tensor fODFs (Definition 3). According to Corollary 1, H is positive semidefinite if and only if the corresponding fODF can be decomposed into a nonnegative

weighted sum of rank-1 terms, which correspond to single fiber compartments in our framework. This provides the theoretical justification of our H-psd constraint, whose practical effectiveness is demonstrated in the main part of the paper.

We represent fODFs as forms or symmetric tensors p of even degree $d = 4$ in $n = 3$ dimensions. In tensor notation:

$$p(\mathbf{x}) = p(\underbrace{\mathbf{x}, \ldots, \mathbf{x}}_{d}) = \sum_{i \in \{1,\ldots,n\}^d} p_{i_1,\ldots,i_d}\, x_{i_1} \ldots x_{i_d}, \quad \mathbf{x} \in \mathbb{R}^n. \tag{7}$$

We will call the set of these forms $F_{n,d}$. Symmetry allows us to use a different, nonredundant indexing scheme

$$p(\mathbf{x}) = \sum_{i \in I(n,d)} \binom{d}{i} p_i\, x^i \tag{8}$$

with multi-indices $i \in I(n,d) = \{i \in {\mathbb{N}_0}^n \,|\, \sum_k i_k = d\}$, multinomial coefficients $\binom{d}{i} = \frac{d!}{\prod i_k!}$ and monomial terms $x^i = \prod_{k=1}^n (x_k)^{i_k}$.

Our constraint stems from the relations of three subsets of $F_{n,d}$:

$$P_{n,d} = \left\{ p \in F_{n,d} : p(\mathbf{x}) \geq 0, \forall\, \mathbf{x} \in \mathbb{R}^n \right\}$$
"positive semidefinite" (9)

$$\Sigma_{n,d} = \left\{ p \in F_{n,d} : p(\mathbf{x}) = \sum_k h_k(\mathbf{x})^2 \right\}$$
"sums of squares" (10)

$$Q_{n,d} = \left\{ p \in F_{n,d} : p(\mathbf{x}) = \sum_k \langle \mathbf{a}_k, \mathbf{x} \rangle^d \right\}$$
"sums of d-th powers" (11)

Here, the $h_k(\mathbf{x})$ denote forms of degree $d/2$, $\mathbf{a}_k$ denote the individual vectors that define the rank-1 terms of a nonnegative decomposition.

As shown in [21], these three subsets obey

$$Q_{n,d} \subset \Sigma_{n,d} \subset P_{n,d}. \tag{12}$$

These sets cannot be vector spaces, since if $p \neq 0$ is positive, $-p$ is not. So the concept of vector spaces has to be weakened:

Definition 1 A convex cone is a subset C of $F_{n,d}$ that obeys:

- $p, q \in C \quad \Rightarrow \quad p + q \in C$
- $p \in C, \lambda \geq 0 \quad \Rightarrow \quad \lambda p \in C$

$P_{n,d}$, $\Sigma_{n,d}$ and $Q_{n,d}$ are closed convex cones.

The definition of our constraint and its properties depend on the choice of a scalar product for forms.

Definition 2 A scalar product on $F_{n,d}$ can be defined as

$$[p, q] = \sum_i \binom{d}{i} p_i\, q_i. \tag{13}$$

For $Q_{n,d}$, this scalar product has a particularly simple form:

Lemma 1 *For $p = \sum_k \langle \boldsymbol{a}_k, \cdot \rangle^d \in Q_{n,d}$ and $q \in F_{n,d}$ we have*

$$[q, p] = \sum_k q(\boldsymbol{a}_k). \tag{14}$$

Proof By the multinomial theorem:

$$\langle \mathbf{a}, \mathbf{x} \rangle^d = \left(\sum_{i=1}^n a_i\, x_i \right)^d = \sum_{i_1 + \cdots + i_n = d} \binom{d}{i} a^i\, x^i \tag{15}$$

And so

$$[q, p] = [q, \sum_k \langle \mathbf{a}_k, \cdot \rangle^d] = \sum_k [q, \langle \mathbf{a}_k, \cdot \rangle^d]$$
$$= \sum_k \sum_i \binom{d}{i} q_i \cdot (a_k)^i = \sum_k q(\mathbf{a}_k).$$

□

Also note that $[\cdot, \cdot]$ corresponds to the usual scalar product for tensors and $[p, p]$ is the square of the Frobenius norm $\|p\|_F$.

In order to derive a matrix representation, we want to reduce a form of even degree $d = 2s$ to $d' = 2$. For this, we need

$$L(\mathbf{x}, t) = \sum_i x^i\, t_i \tag{16}$$

with a vector of variables t indexed by $i \in I(n,s)$. For fixed t, this is a $F_{n,s}$ form in $\mathbf{x}$. For fixed $\mathbf{x}$, this is a linear form in t.

Definition 3 For $p \in F_{n,2s}$, the Hankel form is the quadratic form

$$H_p(t) = [p, L^2(\cdot, t)] = \sum_{i,j} p_{i+j}\, t_i\, t_j \in F_{|I(n,s)|,2}. \tag{17}$$

We can put this into matrix form as $H_p(t) = t^T H_p\, t$. For $p \in F_{3,4}$, the matrix is

$$H_p = \begin{pmatrix} p_{xxxx} & p_{xxxy} & p_{xxxz} & p_{xxyy} & p_{xxyz} & p_{xxzz} \\ p_{xxxy} & p_{xxyy} & p_{xxyz} & p_{xyyy} & p_{xyyz} & p_{xyzz} \\ p_{xxxz} & p_{xxyz} & p_{xxzz} & p_{xyyz} & p_{xyzz} & p_{xzzz} \\ p_{xxyy} & p_{xyyy} & p_{xyyz} & p_{yyyy} & p_{yyyz} & p_{yyzz} \\ p_{xxyz} & p_{xyyz} & p_{xyzz} & p_{yyyz} & p_{yyzz} & p_{yzzz} \\ p_{xxzz} & p_{xyzz} & p_{xzzz} & p_{yyzz} & p_{yzzz} & p_{zzzz} \end{pmatrix}. \tag{18}$$

Definition 4 A form p with positive semidefinite H_p will be called H-psd.

$$H_{n,d} = \{p \in F_{n,d} : H_p(t) \geq 0 \; \forall\, t\} \tag{19}$$

The method we propose enforces the H-psd constraint on fODFs during deconvolution.

In the rest of this section, we will discuss some properties of the set $H_{n,d}$ that are relevant to our method. The main tool will be duality:

Definition 5 The dual cone of a convex cone C is the set

$$C^\star = \{p \in F_{n,d} : [p, q] \geq 0,\ \forall\, q \in C\}. \tag{20}$$

If C is a closed convex cone, then (see Reznick [21])

$$C^{\star\star} = C. \tag{21}$$

Theorem 1 *$P_{n,d}$ and $Q_{n,d}$ are dual to each other:*

$$Q_{n,d}{}^\star = P_{n,d}, \qquad P_{n,d}{}^\star = Q_{n,d} \tag{22}$$

Proof

$$\begin{aligned} p \in Q_{n,d}{}^\star &\iff 0 \leq [q, p] = [\sum_k \langle \mathbf{a}_k, \cdot\rangle^d, p] \\ &= \sum_k p(\mathbf{a}_k), \quad \forall\, q \in Q_{n,d} \\ &\iff 0 \leq p(\mathbf{a}), \quad \forall\, \mathbf{a} \in \mathbb{R}^n \\ &\iff p \in P_{n,d} \end{aligned}$$

The second equation is a consequence of $Q_{n,d}{}^{\star\star} = Q_{n,d}$. □

In the special case of $(n, d) = (3, 4)$, the H-psd constraint is equivalent to decomposability into rank-1 terms. This can be shown with the following two theorems:

Theorem 2 (Hilbert)

$$P_{n,d} = \Sigma_{n,d} \tag{23}$$

if and only if $n = 2$ or $d = 2$ or $(n, d) = (3, 4)$.

Theorem 3

$$\Sigma_{n,d}{}^\star = H_{n,d} \tag{24}$$

Proof Observe that $t \mapsto L(x, t)$ is a bijection between vectors $t \in \mathbb{R}^{|I(n,s)|}$ and forms in $F_{n,s}$. So:

$$\begin{aligned} p \in \Sigma_{n,d}{}^\star &\iff 0 \leq [p, q] = [p, \sum_k h_k^2] \quad \forall\, q \in \Sigma_{n,d} \\ &\iff 0 \leq [p, h^2] \quad \forall\, h \in F_{n,s} \\ &\iff 0 \leq [p, L(\cdot, t)^2] = H_p(t) \quad \forall\, t \in \mathbb{R}^{|I(n,s)|} \end{aligned}$$

□

A direct consequence for $(n, d) = (3, 4)$ is:

Corollary 1 *$p \in F_{3,4}$ is a sum of fourth powers iff it is H-psd, since*

$$Q_{3,4} = P_{3,4}{}^\star = \Sigma_{3,4}{}^\star = H_{3,4}. \tag{25}$$

For higher degrees, the relation is weaker:

$$Q_{3,n} \subsetneq H_{3,n} \subset P_{3,n} \tag{26}$$

Another property of the H matrix is that it can be used to estimate the number of fibers in an fODF.

Definition 6 The rank of $p \in Q_{n,d}$ is the smallest integer $\mathrm{rank}(p) = r$ for which $\mathbf{a}_1, \ldots, \mathbf{a}_r \in \mathbb{R}^n$ can be found with

$$p = \sum_{k=1}^{r} \langle \mathbf{a}_k, \cdot\rangle^d. \tag{27}$$

For the cases in Hilbert's Theorem 2, the ranks of p and H_p are equal as shown in theorem 4.6 in [21]. In general, $\mathrm{rank}(p) \geq \mathrm{rank}(H_p)$.

References

1. Andersson JLR, Sotiropoulos SN (2016) An integrated approach to correction for off-resonance effects and subject movement in diffusion mr imaging. NeuroImage 125:1063–1078
2. Ankele M, Lim LH, Groeschel S, Schultz T (2016) Fast and accurate multi-tissue deconvolution using SHORE and H-psd tensors. In: Proceedings of medical image analysis and computer-aided intervention (MICCAI) part III, LNCS, vol 9902. Springer, Berlin, pp 502–510
3. Basser PJ, Pajevic S, Pierpaoli C, Duda J, Aldroubi A (2000) In vivo fiber tractography using DT-MRI data. Magn Reson Med 44:625–632
4. Canales-Rodríguez EJ, Iturria-Medina Y, Alemán-Gómez Y, Melie-García L (2010) Deconvolution in diffusion spectrum imaging. NeuroImage 50:136–149

5. Chen Z, Tie Y, Olubiyi O, Zhang F, Mehrtash A, Rigolo L, Kahali P, Norton I, Pasternak O, Rathi Y, Golby AJ, O'Donnell LJ (2016) Corticospinal tract modeling for neurosurgical planning by tracking through regions of peritumoral edema and crossing fibers using two-tensor unscented kalman filter tractography. Int J Comput Assist Radiol Surg 11(8):1475–1486
6. Cheng J, Deriche R, Jiang T, Shen D, Yap PT (2014) Non-negative spherical deconvolution (NNSD) for estimation of fiber orientation distribution function in single-/multi-shell diffusion MRI. NeuroImage 101:750–764
7. Christiaens D, Sunaert S, Suetens P, Maes F (2016) Convexity-constrained and nonnegativity-constrained spherical factorization in diffusion-weighted imaging. NeuroImage 146:507–517. doi:10.1016/j.neuroimage.2016.10.040
8. Descoteaux M, Deriche R, Knösche TR, Anwander A (2009) Deterministic and probabilistic tractography based on complex fibre orientation distributions. IEEE Trans Med Imaging 28(2):269–286
9. Garyfallidis E, Brett M, Amirbekian B, Rokem A, Van Der Walt S, Descoteaux M, Nimmo-Smith I (2014) Dipy, a library for the analysis of diffusion MRI data. Front Neuroinform. 8(8). doi:10.3389/fninf.2014.00008
10. Jeurissen B, Tournier JD, Dhollander T, Connelly A, Sijbers J (2014) Multi-tissue constrained spherical deconvolution for improved analysis of multi-shell diffusion MRI data. NeuroImage 103:411–426
11. Jiao F, Gur Y, Johnson CR, Joshi S (2011) Detection of crossing white matter fibers with high-order tensors and rank-*k* decompositions. In: Székely G, Hahn HK (eds) IPMI, LNCS, vol 6801, pp 538–549
12. Jones DK, Knösche TR, Turner R (2013) White matter integrity, fiber count, and other fallacies: the do's and don'ts of diffusion MRI. NeuroImage 73:239–254
13. Knutsson H, Westin CF (2013) Tensor metrics and charged containers for 3d q-space sample distribution. In: Mori K, Sakuma I, Sato Y, Barillot C, Navab N (eds) Proceedings of medical image computing and computer-assisted intervention (MICCAI) part I, LNCS, vol 8149, Springer, Berlin, pp 679–686
14. Malcolm JG, Michailovich O, Bouix S, Westin CF, Shenton ME, Rathi Y (2010) A filtered approach to neural tractography using the Watson directional function. Med Image Anal 14:58–69
15. Merlet SL, Deriche R (2013) Continuous diffusion signal, EAP and ODF estimation via compressive sensing in diffusion MRI. Med Image Anal 17:556–572
16. Mori S, Crain BJ, Chacko VP, van Zijl PCM (1999) Three-dimensional tracking of axonal projections in the brain by magnetic resonance imaging. Ann Neurol 45(2):265–269
17. Özarslan E, Mareci T (2003) Generalized diffusion tensor imaging and analytical relationships between diffusion tensor imaging and high angular resolution diffusion imaging. Magn Reson Med 50:955–965
18. Paquette M, Merlet S, Gilbert G, Deriche R, Descoteaux M (2015) Comparison of sampling strategies and sparsifying transforms to improve compressed sensing diffusion spectrum imaging. Magn Reson Med 73(1):401–416
19. Raffelt D, Tournier JD, Rose S, Ridgway GR, Henderson R, Crozier S, Salvado O, Connelly A (2012) Apparent fibre density: a novel measure for the analysis of diffusion-weighted magnetic resonance images. NeuroImage 59(4):3976–3994
20. Reisert M, Mader I, Anastasopoulos C, Weigel M, Schnell S, Kiselev V (2011) Global fiber reconstruction becomes practical. NeuroImage 54(2):955–962
21. Reznick B (1992) Sums of even powers of real linear forms. American Mathematical Society
22. Schultz T, Fuster A, Ghosh A, Deriche R, Florack L, Lim LH (2014) Higher-order tensors in diffusion imaging. In: Westin CF, Vilanova A, Burgeth B (eds) Visualization and processing of tensors and higher order descriptors for multi-valued data. Springer, Berlin, pp 129–161
23. Schultz T, Groeschel S (2013) Auto-calibrating spherical deconvolution based on ODF sparsity. In: Mori K, Sakuma I, Sato Y, Barillot C, Navab N (eds) Proceedings of medical image computing and computer-assisted intervention (MICCAI) part I, LNCS, vol 8149. Springer, Berlin, pp 663–670
24. Schultz T, Seidel HP (2008) Estimating crossing fibers: a tensor decomposition approach. IEEE Trans Vis Comput Gr 14(6):1635–1642
25. Tournier JD, Calamante F, Connelly A (2010) Improved probabilistic streamlines tractography by 2nd order integration over fiber orientation distributions. In: Proceedings of international society of magnetic resonance in medicine (ISMRM), p 1670
26. Tournier JD, Calamante F, Connelly A (2007) Robust determination of the fibre orientation distribution in diffusion MRI: non-negativity constrained super-resolved spherical deconvolution. NeuroImage 35:1459–1472
27. Tournier JD, Calamante F, Connelly A (2012) MRtrix: diffusion tractography in crossing fiber regions. Int J Imaging Syst Technol 22(1):53–66
28. Tournier JD, Calamante F, Gadian DG, Connelly A (2004) Direct estimation of the fiber orientation density function from diffusion-weighted MRI data using spherical deconvolution. NeuroImage 23:1176–1185
29. Vandenberghe L (2010) The CVXOPT linear and quadratic cone program solvers. Tech. rep., UCLA Electrical Engineering Department. http://www.seas.ucla.edu/~vandenbe/publications/coneprog.pdf
30. Wedeen V, Wang R, Schmahmann J, Benner T, Tseng W, Dai G, Pandya D, Hagmann P, D'Arceuil H, de Crespigny A (2008) Diffusion spectrum magnetic resonance imaging (DSI) tractography of crossing fibers. NeuroImage 41(4):1267–1277
31. Wedeen VJ, Hagmann P, Tseng WYI, Reese TG, Weisskoff RM (2005) Mapping complex tissue architecture with diffusion spectrum magnetic resonance imaging. Magn Reson Med 54(6):1377–1386
32. Wedeen VJ, Rosene DL, Wang R, Dai G, Mortazavi F, Hagmann P, Kaas JH, Tseng WYI (2012) The geometric structure of the brain fiber pathways. Science 335(6076):1628–1634
33. Weldeselassie YT, Barmpoutis A, Atkins MS (2012) Symmetric positive semi-definite cartesian tensor fiber orientation distributions (CT-FOD). Med Image Anal 16(6):1121–1129
34. Zhang Y, Brady M, Smith S (2001) Segmentation of brain MR images through a hidden markov random field model and the expectation-maximization algorithm. IEEE Trans Med Imaging 20(1):45–57